

Article

Dynamic Inversion Method of Calculating Large-Scale Urban Building Height Based on Cooperative Satellite Laser Altimetry and Multi-Source Optical Remote Sensing

Haobin Xia ¹, Jianjun Wu ^{1,2,*}, Jiaqi Yao ^{1,*} , Nan Xu ^{3,4} , Xiaoming Gao ⁵, Yubin Liang ¹, Jianhua Yang ¹, Jianhang Zhang ², Liang Gao ¹, Weiqi Jin ¹ and Bowen Ni ¹

- ¹ Academy of Eco-Civilization Development for Jing-Jin-Ji Megalopolis, Tianjin Normal University, Tianjin 300387, China; 2210080045@stu.tjnu.edu.cn (H.X.); ybliang@tjnu.edu.cn (Y.L.); yangjh15@mail.bnu.edu.cn (J.Y.); 2300080006@stu.tjnu.edu.cn (L.G.); 2310080041@stu.tjnu.edu.cn (W.J.); 2310080046@stu.tjnu.edu.cn (B.N.)
- ² Faculty of Geographical Science, Beijing Normal University, Beijing 100875, China; 202121051093@mail.bnu.edu.cn
- ³ Department of Land Surveying and Geo-Informatics, The Hong Kong Polytechnic University, Hong Kong, China; 20220134@hku.edu.cn
- ⁴ College of Geography and Remote Sensing, Hohai University, Nanjing 211100, China
- ⁵ Land Satellite Remote Sensing Application Center, Ministry of Natural Resources, Beijing 100048, China; gaoxm@lasac.cn
- * Correspondence: jjwu@bnu.edu.cn (J.W.); yaojiaqi@tjnu.edu.cn (J.Y.)

Abstract: Building height is a crucial indicator when studying urban environments and human activities, necessitating accurate, large-scale, and fine-resolution calculations. However, mainstream machine learning-based methods for inferring building heights face numerous challenges, including limited sample data and slow update frequencies. Alternatively, satellite laser altimetry technology offers a reliable means of calculating building heights with high precision. Here, we initially calculated building heights along satellite orbits based on building-rooftop contour vector datasets and ICESat-2 ATL03 photon data from 2019 to 2022. By integrating multi-source passive remote sensing observation data, we used the inferred building height results as reference data to train a random forest model, regressing building heights at a 10 m scale. Compared with ground-measured heights, building height samples constructed from ICESat-2 photon data outperformed methods that indirectly infer building heights using total building floor number. Moreover, the simulated building heights strongly correlated with actual observations at a single-city scale. Finally, using several years of inferred results, we analyzed building height changes in Tianjin from 2019 to 2022. Combined with the random forest model, the proposed model enables large-scale, high-precision inference of building heights with frequent updates, which has significant implications for global dynamic observation of urban three-dimensional features.

Keywords: satellite laser altimetry; ICESat-2; building height; random forest; Sentinel-1; Sentinel-2; VIIRS; dynamic monitoring



Citation: Xia, H.; Wu, J.; Yao, J.; Xu, N.; Gao, X.; Liang, Y.; Yang, J.; Zhang, J.; Gao, L.; Jin, W.; et al. Dynamic Inversion Method of Calculating Large-Scale Urban Building Height Based on Cooperative Satellite Laser Altimetry and Multi-Source Optical Remote Sensing. *Land* **2024**, *13*, 1120. <https://doi.org/10.3390/land13081120>

Academic Editor: Deodato Tapete

Received: 13 May 2024

Revised: 14 July 2024

Accepted: 20 July 2024

Published: 24 July 2024



Copyright: © 2024 by the authors. Licensee MDPI, Basel, Switzerland. This article is an open access article distributed under the terms and conditions of the Creative Commons Attribution (CC BY) license (<https://creativecommons.org/licenses/by/4.0/>).

1. Introduction

High-precision urban three-dimensional (3D) information serves as a critical reference for tasks such as urban planning, emergency management, and autonomous driving [1–3] and forms the foundation for further advancements in technologies such as city information models and 3D real scenes [4,5]. Building heights constitute a principal geographical element in urban 3D morphology and are important indicators of complex systems involving urbanization, heat island effects, and human–environment interactions. Therefore, achieving long-term, large-scale, and highly accurate extraction of building heights is of considerable importance [6–9].

Numerous methods exist for acquiring 2D building outlines; however, obtaining high-precision height data remains challenging. Currently, the widely used methods for building height extraction fall into three main categories [10–13]: (1) 3D laser scanning technology, (2) oblique photogrammetry, and (3) satellite stereo-mapping technology. Three-dimensional laser scanning and oblique photogrammetry rapidly capture high-precision building height information using unmanned aerial vehicles (UAVs). However, these technologies are constrained by external environmental factors, flight restrictions, and high costs, rendering it difficult to satisfy the demands of large-scale urban applications [14–16]. Alternatively, with the rapid development of Earth observation technologies, satellite stereo mapping employing dual- or triple-line mapping cameras for the large-scale stereoscopic mapping of areas has emerged as a dominant means of acquiring global building heights because of its high spatial and temporal resolution, extensive coverage, and ready data accessibility [17–19]. Nevertheless, issues such as clouds and fog obscuring image quality, reliance on prior control points, and the poor precision of elevation inversion hinder its direct application to height extraction in densely built areas [16,20,21].

The ICESat-2 satellite, launched in 2018, is the first to carry the multi-beam photon-counting light detection and ranging (LiDAR) Advanced Topographic Laser Altimeter System (ATLAS), enabling direct acquisition of elevation profiles along its track over urban areas. However, realizing the large-scale, high-precision, and automated extraction of building heights in complex scenes presents numerous technical challenges [22]. Although ICESat-2 can generate vast amounts of photon point-cloud data in a short timeframe, these data are contaminated by substantial background noise. Density-based spatial clustering, local distance statistics, and machine learning theories have been employed to differentiate and remove noise based on the differences in spatial distribution [23–26]. Although these algorithms are not optimal for processing building photons given the significant variations in vertical photon distributions across different ground types [27–29], an overall accuracy of building height measurements of up to 1.5 m has been attained using the ICESat-2 ATL03 product in dense urban areas [30,31]. Moreover, local precision has been further improved to 8–17 cm by adopting a strategy of selecting building heights based on height differences between adjacent photons in small regions. However, this threshold approach has substantial limitations in broader applications [32]. Furthermore, relying solely on along-track elevation profiles for building height extraction introduces some uncertainty stemming from factors such as measurement errors caused by complex terrain within the laser spot footprint and potential forward-scattering effects along the laser transmission path [33–35].

Against this backdrop, research institutions such as the United States National Aeronautics and Space Administration (NASA) have explicitly outlined their decadal development plans for surface 3D mapping, including technological advances such as the Concurrent Artificially Intelligent Spectrometry and Adaptive LiDAR System (CASALS). This system was designed to integrate advanced spectral cameras and LiDARs to acquire cross-orbit, true 3D information and enhance the understanding of the drivers and processes underlying height variations [36]. Achieving accurate identification of 3D building features through the fusion of active and passive satellite sensors and multi-source reference data is an inevitable trend in current mainstream technology. For example, Zhao et al. [37] combined ICESat-2 and Google Earth image data to propose a deep learning height estimation model based on building shadows and offset distances; however, such methods require an azimuth angle between the sensor and the sun to both deviate from the nadir and be $<180^\circ$ [37–39]. Wu et al. [38] utilized building floor count data from Baidu Maps and Earth observation data to develop a random forest-based building height prediction model using a joint shadow index, achieving height inversion at a 10 m resolution. However, the building height samples were constructed by multiplying the building floor counts by an assumed floor height of 3 m, resulting in lower accuracy. Furthermore, this method relies solely on data from the year 2020, precluding the longitudinal observations of building height dynamics over multiple years.

To address the issues of limited sample data, low precision, and slow update frequency in the existing building height footprint research, in this study, we utilized the ICESat-2 ATL03 product combined with building rooftop vector data to construct annual building height samples for Tianjin, China as a representative large, complex urban area. Through integrating these samples with multi-source remote sensing data, a random forest model was employed to derive 10 m resolution building heights for the period 2019–2022. Studying the overall building heights of such megacities offers critical insights regarding the dynamics of urban structures, highlighting the significance of these data for academic research and urban planning. Moreover, the developed building height inversion methodology transcends the temporal and spatial constraints of previous approaches, and has profound implications for the dynamic monitoring of urban 3D structures on a global scale.

2. Materials and Methods

2.1. Overview of the Study Area

Tianjin, one of the four municipalities directly under the Central Government of China, is a typical megacity with a permanent population of 13,630,000 individuals and covers an area of 11,966.45 km². It is located along the coast of Bohai Bay in North China and features flat terrain and convenient transportation, making it the largest port city in northern China and an important component of the Jing-Jin-Ji metropolitan region. The city's economy is vibrant and is divided into six core districts: Heping, Hexi, Hedong, Hebei, Nankai, Hongqiao, and 10 other districts: Binhai New Area, Jinnan, Xiqing, Beichen, Dongli, Baodi, Wuqing, Jinghai, Ninghe, and Jizhou. Densely built areas account for approximately 8.25% of Tianjin's total area. The old city area, with its long history, hosts a multitude of modern as well as historic structures, whereas new city areas are predominantly modern and include many rural buildings. Overall, Tianjin boasts a rich variety of building types along with differing construction rates between its core and other districts, providing an excellent research setting for observing urban dynamics.

2.2. Data Collection

We employed multi-source remote sensing data from various satellites, including ICESat-2, Sentinel-1, Sentinel-2, and National Oceanic and Atmospheric Administration (NOAA)/Visible Infrared Imaging Radiometer Suite (VIIRS). We also utilized multiple reference datasets, such as Vectorized Rooftop Area Data for 90 Cities in China [38] and the 90 m-resolution Global Digital Elevation Model (DEM) product Shuttle Radar Topography Mission (SRTM).

2.2.1. ICESat-2

We utilized the ICESat-2 onboard photon counter to invert building heights. Equipped with ATLAS, ICESat-2 operates at a 532 nm wavelength using an emitter, sensitive receiver, and high-precision timing system. ATLAS fires three pairs of laser beams, spaced 3.3 km apart along-track with an intra-pair separation of 90 m, at a repetition rate of 10 kHz, scanning the Earth's surface and producing overlapping footprints 17 m in diameter every 0.7 m. Each pair consists of a strong and a weak beam in a 4:1 energy ratio, as depicted in Figure 1a. Compared with the measures from the Geoscience Laser Altimeter System (GLAS) aboard ICESat-1, ATLAS significantly increases the ground track density and coverage area. Whereas ICESat-2 is primarily designed for generating geophysical products for various surface types, such as land ice (ATL06), sea ice (ATL07), land/vegetation (ATL08), atmosphere (ATL09), ocean (ATL12), and inland waters (ATL13), it also offers measurements over densely built regions, enabling the estimation of urban building heights [32]. As shown in Figure 1b, the laser footprints form a two-dimensional profile distribution along the orbit; however, ATLAS is susceptible to background noise, with signal photons that are not directly distinguishable from noise photons [32]. Nonetheless, the strong energy reflected from both the ground and building tops results in significantly higher photon

densities than those obtained from ICESat-1 regardless of beam strength. Leveraging this characteristic allows the separation of signal photons from noise photons.

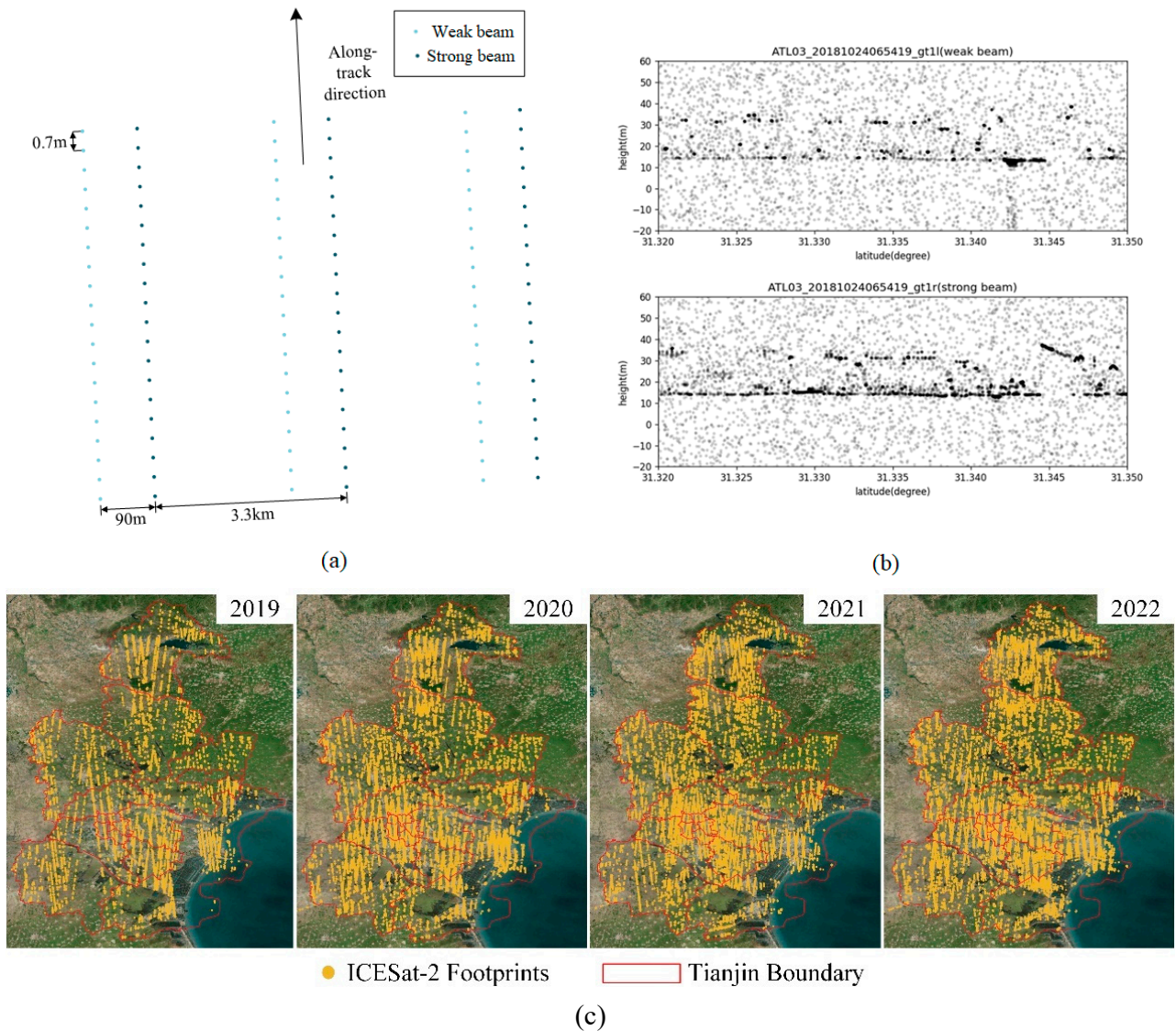


Figure 1. ICESat-2 photon data. (a) Basic distribution of ICESat-2 data. (b) Distribution of photons from a pair of strong and weak beams in the ICESat-2 data in the along-track direction. (c) Distribution of ICESat-2 data in the Tianjin area.

A substantial amount of ICESat-2 footprint data is available for the Tianjin region from 2019 to 2022, as illustrated in Figure 1c, which covers all major urban areas within the Tianjin Municipality. This extensive coverage provides a robust foundation for constructing a uniform and comprehensive sample of building heights. Although the number of footprints in 2019 is relatively low, a marked increase in footprint density can be observed in the subsequent three years.

2.2.2. Other Datasets

As presented in Table 1, additional data sources utilized to estimate building heights included vectorized rooftop area, synthetic aperture radar (SAR), multispectral imagery, nighttime light, reference terrain, and UAV photogrammetry data. The detailed characteristics of each dataset are listed in Table 1.

The Vectorized Rooftop Area Data for 90 Cities in China [38,40] provided a detailed vector representation of building rooftops in Tianjin, which served as a valuable spatial ref-

erence for processing the ICESat-2 photon data. The overall accuracy of this dataset reached 97.95%. This dataset ensured that the analysis was focused on the targeted buildings within the city, facilitating accurate interpretation and integration of the ICESat-2 measurements.

Table 1. Other datasets used to estimate building height.

Data Type	Dataset Name	Temporal Range and Spatial Resolution	Involved Indicators
Building outline vector	Vectorized Rooftop Area Data for 90 Cities in China	2020	
Synthetic Aperture Radar	Sentinel-1 GRD	2019–2022 10 m	$VVH = VV * \gamma^{VH}$ (1)
Multispectral	Sentinel-2	2019–2022 10 m	$NDVI = \frac{\rho_{NIR} - \rho_{Red}}{\rho_{NIR} + \rho_{Red}}$ (2)
			$EVI = \frac{2.5 * (\rho_{NIR} - \rho_{Red})}{\rho_{NIR} + 6 * \rho_{Red} - 7.5 * \rho_{Blue} + 1}$ (3)
			$LWSI = \frac{\rho_{NIR} - \rho_{swir1}}{\rho_{NIR} + \rho_{swir1}}$ (4)
			$MNDWI = \frac{\rho_{Green} - \rho_{swir1}}{\rho_{Green} + \rho_{swir1}}$ (5)
			$NDBI = \frac{\rho_{swir1} - \rho_{NIR}}{\rho_{swir1} + \rho_{NIR}}$ (6)
			$SEI = \frac{(\rho_{Aerosols} + \rho_{Vapor}) - (\rho_{Green} + \rho_{NIR})}{(\rho_{Aerosols} + \rho_{Vapor}) + (\rho_{Green} + \rho_{NIR})}$ (7)
			$CSI = \begin{cases} SEI - \rho_{NIR}, & \text{if } \rho_{NIR} > NDWI \\ SEI - NDWI, & \text{else} \end{cases}$ (8)
Infrared	NOAA/VIIRS	2019–2022 500 m	
Reference terrain	SRTM	2000 90 m	$slope = \frac{\Delta H}{\Delta D} * 100\%$ (9)
Validation	UAV Photogrammetry	2021.5 0.15 m	

NOAA, National Oceanic and Atmospheric Administration; VIIRS, Visible Infrared Imaging Radiometer Suite; GRD, ground range detected; SRTM, Shuttle Radar Topography Mission; UAV, unmanned aerial vehicles.

2.3. Methods

2.3.1. Study Design

The research methodology was divided into three main parts. The first part involved constructing high-precision building height sample data for Tianjin City over different time periods based on ICESat-2 and building rooftop contour vector datasets. In the second part, urban building heights were retrieved by integrating the constructed sample data with multi-source passive remote sensing data. In the third part, we analyzed the dynamic changes in urban building heights based on the retrieved building height results. Figure 2 illustrates the main technical framework and workflow of this study.

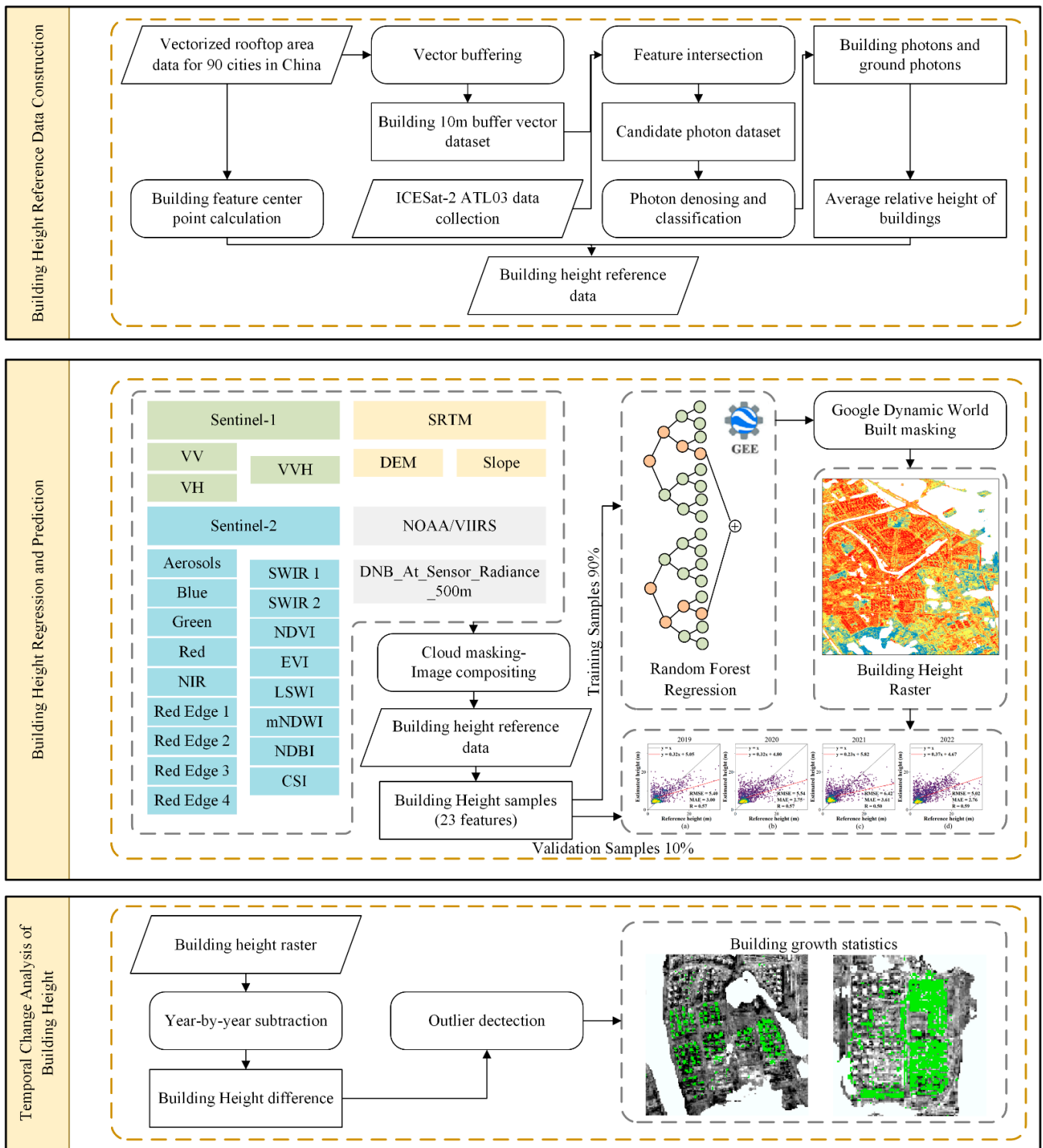


Figure 2. Technical framework of the study. VV, vertical–vertical polarization; VH, vertical–horizontal polarization; VVH, --; SRTM, Shuttle Radar Topography Mission; DEM, digital elevation model; SWIR, short-wave infrared; NDVI, normalized difference vegetation index; EVI, Landsat enhanced vegetation index; LSWI, land surface water index; mNDWI, modified normalized difference water index; NDBI, normalized difference built-up index; CSI, combination shadow index; NOAA, National Oceanic and Atmospheric Administration; VIIRS, Visible Infrared Imaging Radiometer Suite.

2.3.2. Building Height Reference Data Construction

The ICESat-2 ATL03 product alone does not directly yield building heights and contains substantial background noise photons. Thus, the relative heights of buildings must be estimated, which requires concurrent knowledge of both the building and surrounding terrain elevations, and the photon data denoised. As illustrated in Figure 3a, the orbital length passing through the administrative districts of Tianjin City was extensive, resulting in large data volumes and complex situations that hampered direct processing. In contrast, the spatial extent of the photon data at the individual building level is much smaller, which simplifies the analysis. To obtain photon data for each building and its surroundings, we relied on a vector dataset of building rooftop contours to create 10 m buffers, with the photon data falling within each buffer being selected and labeled with building contour numbers for subsequent retrieval and processing. The filtered photon data are shown in Figure 3b. Taking building No. 1180964 as an example, as shown in Figure 3c, the photons within the building's range exhibit a distinct bimodal distribution, characteristic of separation between the ground and roof. Typically, building tops are smooth and continuous, as shown in Figure 3d, allowing for the identification of the absolute heights of building tops in local areas, which, combined with the surrounding ground photon heights, enables the calculation of building relative heights. Given the positional error of photons, we computed the average building height within the building area using photons from both the buffer area and ground, which served as the overall building height and mitigated the issue of positional error to some extent.

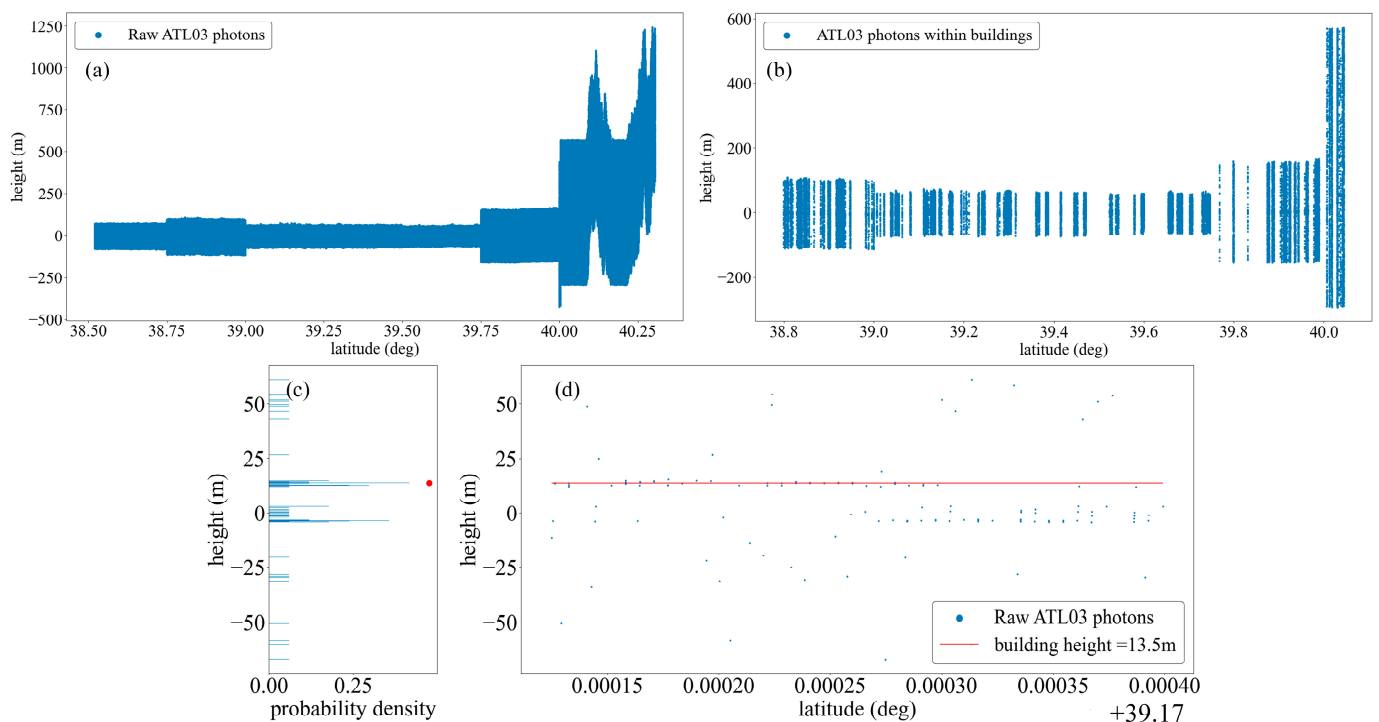


Figure 3. ICESat-2 photon data. (a) Orbital data of building photons passing through Tianjin on 9 November 2018. (b) Remaining building photons intersecting the building contours along the orbit. (c) Distribution of building photons within the buffer of Building No. 1180964. (d) The red line represents the plane of the top of the building.

We applied a two-step approach for denoising. First, DBSCAN was used to remove the majority of the background noise, as DBSCAN has been reported to eliminate $\geq 90\%$ of noise photons. Second, the denoising was enhanced on the basis that buildings and ground surfaces within small local areas are relatively flat and often approximated as straight

lines. Accordingly, the RANSAC line-fitting algorithm was applied to each point cluster to remove photons that deviated significantly from the fitted line.

Specifically, the relative building height reference data were established as follows. In most scenarios, the height of the buildings should exceed 1.5 m. Within the 10 m buffer range formed by the vector scope of a given building, the two ends should encompass the surrounding ground. Therefore, the two end clusters should represent ground photons. Based on this premise, photon clusters that were 1.5 m higher than these ground photon clusters were considered building photon clusters.

We then directly computed the relative height of buildings by subtracting the average height of the ground clusters from that of the building clusters. However, during actual calculations, both remote sensing imagery and ICESat-2 data may exhibit some horizontal errors and may be influenced by thin clouds, leading to situations in which a building vector zone lacks distinct clusters with a 1.5 m height difference. The building height calculations for these vectors were omitted. Upon obtaining the building heights, the centroid of the vector polygons was computed, and the inverted building height results were assigned to these points, serving as sample points for sampling.

The detailed steps of the denoising method are illustrated in Figure 4. In the first step, the DBSCAN algorithm with a tolerance of 2.1 m is used for noise identification. This distance is approximately the horizontal spacing of three ICESat-2 spots, allowing for the elimination of approximately 90% of stray noise, as illustrated in Figure 4b. In the second step, the DBSCAN algorithm with a tolerance of 1.4 m, which is equivalent to the horizontal spacing of two spots, is used for further denoising. This step removes small clusters that deviate from the main objects, as illustrated in Figure 4c, thereby further reducing interference. Finally, RANSAC linear fitting is applied to remove points whose perpendicular distance from the fitted line exceeds three times the standard deviation of the outliers. This ensures that all points are essentially aligned along a single line, consistent with the characteristics of building rooftops and the nearby ground, as illustrated in Figure 4d.

To verify the reliability of the results, we employed the Pearson correlation coefficient (R), root mean square error ($RMSE$), and mean absolute error (MAE) as metrics (defined below) to assess the precision of the results.

$$R = \frac{\sum_{i=1}^n cov(H_i, \hat{H}_i)}{\sum_{i=1}^n \sqrt{D(H_i)} * \sqrt{D(\hat{H}_i)}}, \quad (10)$$

$$RMSE = \sqrt{\frac{1}{n} \sum_{i=1}^n (H_i - \hat{H}_i)^2}, \quad (11)$$

$$MAE = \frac{1}{n} \sum_{i=1}^n |H_i - \hat{H}_i|, \quad (12)$$

where H_i, \hat{H}_i represent the true and predicted values of building height, respectively.

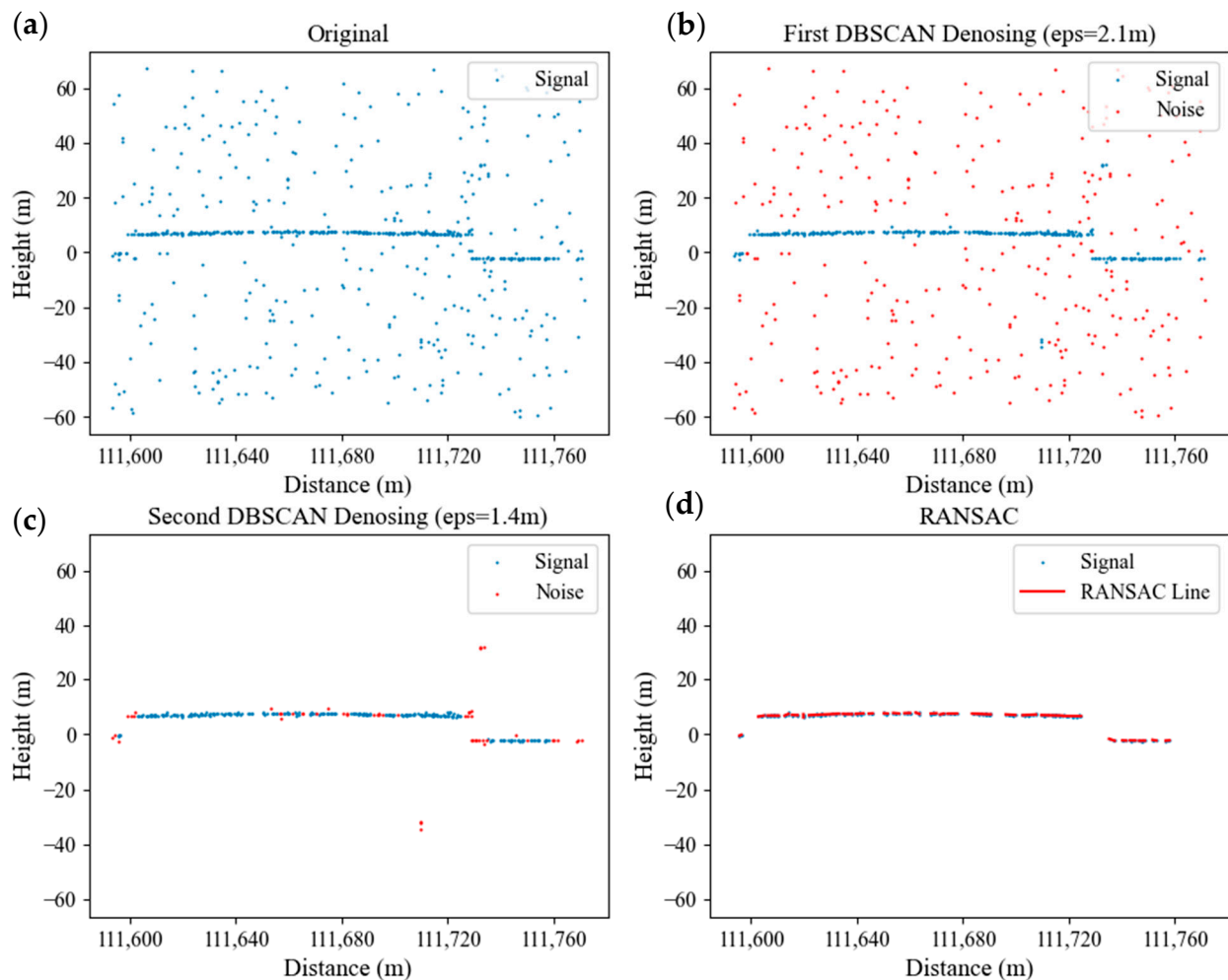


Figure 4. Denoising steps. (a) Original signals from ICESat-2 ATL03. (b) The denoising process generally involves first performing DBSCAN denoising with a tolerance of 2.1m. The red points represent noise identified by the algorithm, while the blue dots represent the signals retained by the algorithm. (c) The following involves DBSCAN denoising with a tolerance of 1.4m. Points with fewer than 4 remaining are removed in this step. (d) Finally, RANSAC line fitting is performed to eliminate other noise points. The red line is the fitting line of the RANSAC linear algorithm, and the blue dots represent the signals within a certain range of the line.

2.3.3. Building Height Estimation

To estimate building height, we first conducted cloud masking on Sentinel-2 optical imagery by employing the Google Earth Engine (GEE) platform to eliminate pixels with cloud coverage surpassing 60%. The GEE platform further computed the annual means for Sentinel-1, Sentinel-2, and VIIRS data to fill any gaps, thereby mitigating interannual fluctuations in the data features. Moreover, additional indices were generated from partial data to serve as input variables. The VIIRS and SRTM datasets were also resampled at 10 m resolution to achieve consistency across the datasets.

We adopted a random forest regression model as the fundamental framework for building height inversion. In this model, the two critical parameters are the number of trees (NTrees) and number of features per binary tree node (Mtry). NTrees directly influences the performance of the random forest regression model; however, the model's inherent regression mechanism effectively prevents overfitting, allowing this value to be set relatively high. In this study, NTree was set to 500 because the model error stabilized prior to reaching this parameter value. In addition, the magnitude of Mtry affects the model's consideration of features. When Mtry is small, some highly influential key variables may

be neglected, whereas when it is large, the model's responsiveness to individual feature variables diminishes. Drawing on established training practices, this value was customarily set as the square root of the number of features. The random forest model employed in this study was constructed using the GEE platform.

3. Results and Discussion

3.1. Building Height Estimation Based on Satellite Altimetry Data

Using building contour data from 2021 as the basis, we estimated building height data for the Tianjin area for 2019, 2020, 2021, and 2022, successfully determining the heights of 11,968, 20,032, 17,409, and 21,203 structures, respectively. These derived datasets served as reference inputs for subsequent random forest-based inversion analyses. To assess the accuracy of the derived building height reference data, they were compared with the data of digital surface models generated through UAV oblique photogrammetry for a set of seven distinct buildings (Table 2). The geographical distributions of the seven selected buildings are shown in Figure 5.

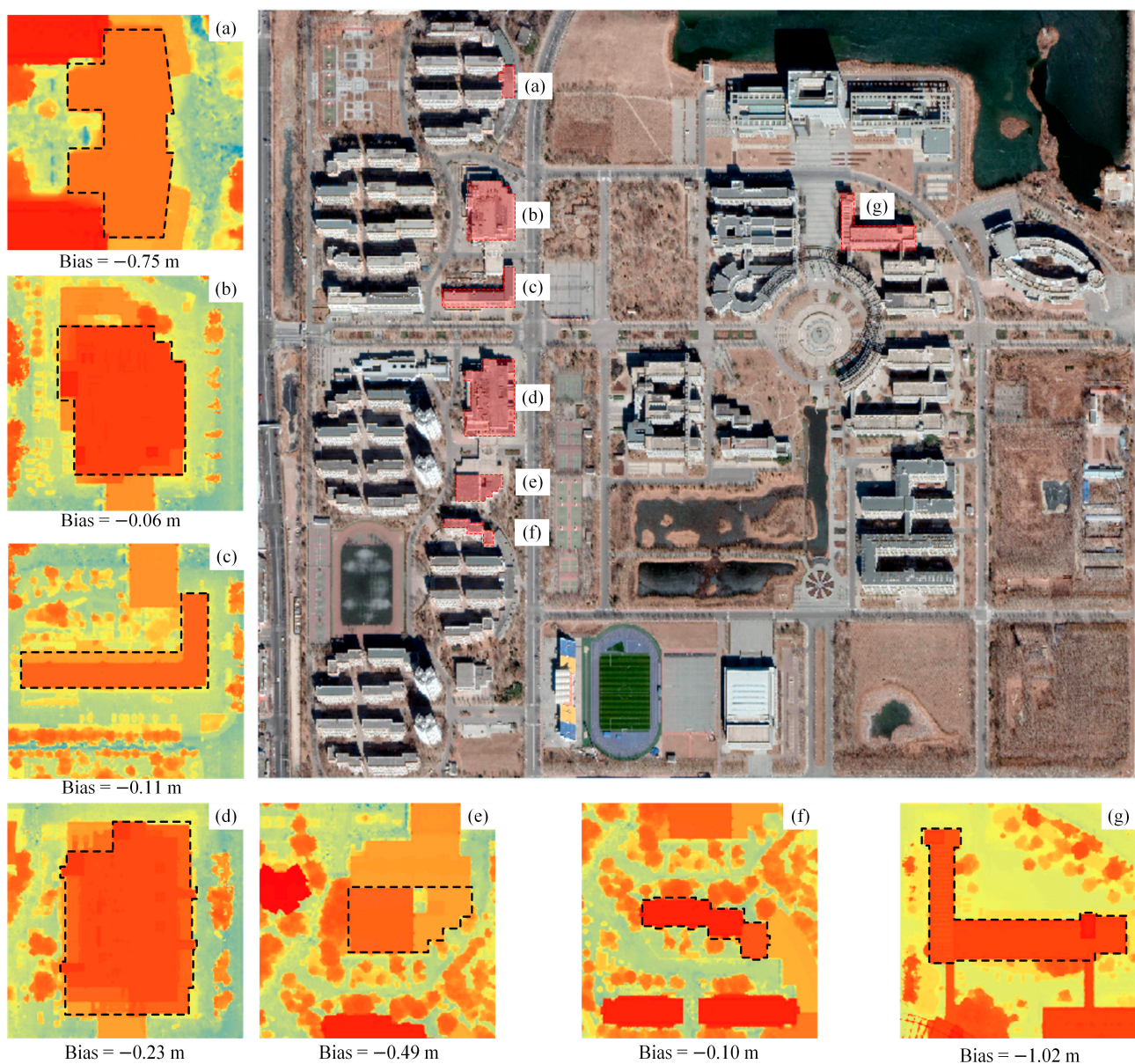


Figure 5. Validation using unmanned aerial vehicle ground data. (a–g) Digital surface model results of the seven indicated buildings covered by ICESat-2 satellite data.

Table 2. ICESat-2-retrieved heights vs. UAV photogrammetry-modeled heights.

Point Index	Height from ICESat-2 (m)	Height from UAV (m)	Bias (m)
1	20.77	20.83	−0.06
2	5.79	6.54	−0.75
3	10.40	10.29	0.11
4	19.41	19.18	0.23
5	10.83	11.32	−0.49
6	21.19	21.29	−0.10
7	15.78	16.80	−1.02

The results indicate that building heights inferred from ICESat-2 data exhibit a high level of accuracy, with a maximum error of -1.02 m. This specific error is largely due to the substantial size and irregular topography of the relevant building, with the ICESat-2 laser footprint only covering one side of the edifice, resulting in a substantial deviation in the height estimation. In contrast, the majority of building samples display errors confined within the range of ± 0.5 m. Notably, the heights obtained from ICESat-2 demonstrate enhanced precision and reliability relative to the reference data derived from indirectly inferred building heights using Baidu floor-level data [41].

3.2. Building Height Results Derived from Multi-Source Remote Sensing Data Regression

Using building height reference data from different years, we constructed a sample dataset employing annual Sentinel-1, Sentinel-2, and VIIRS remote sensing data along with SRTM digital elevation model raster data to train a random forest regression model to estimate building heights in the Tianjin region. The inversion results are shown in Figure 6.

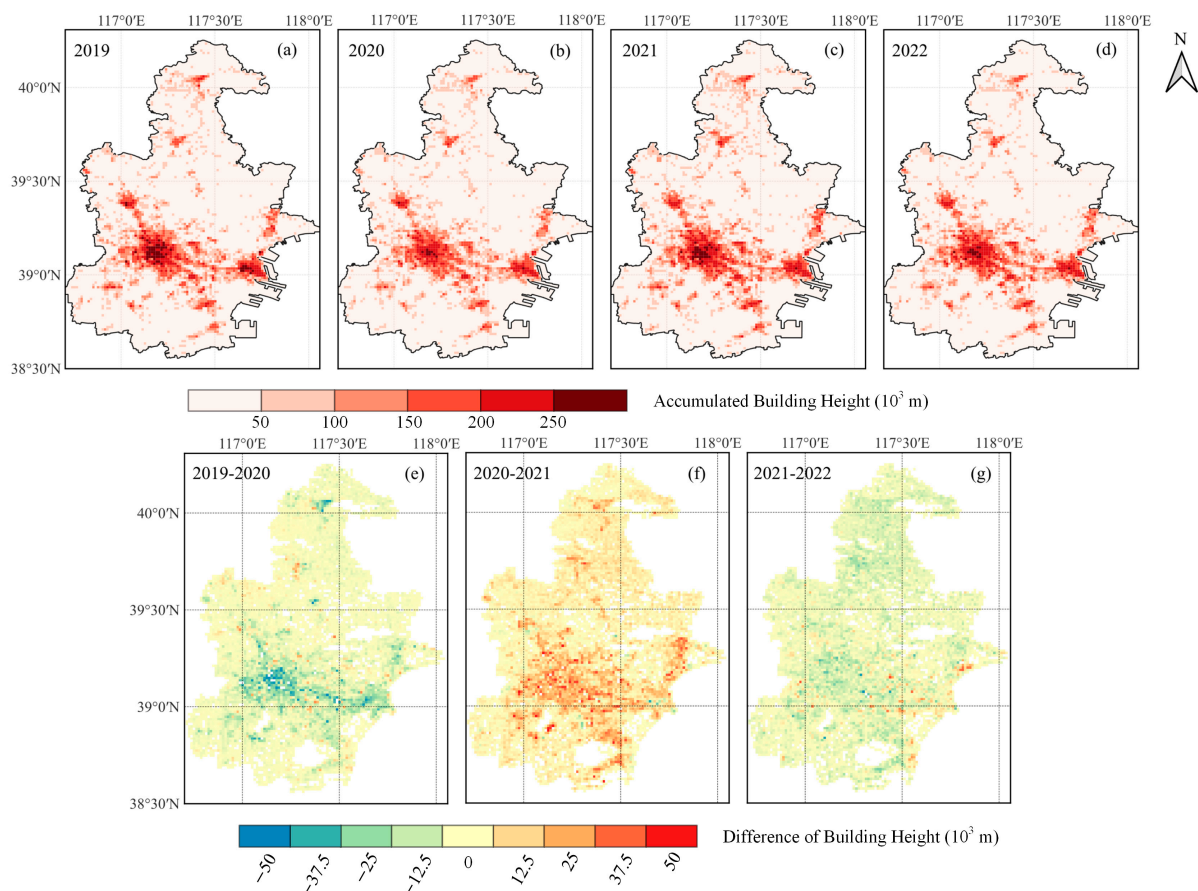


Figure 6. Building height results for Tianjin from 2019 through 2022. (a–d) Accumulated building height for each year. (e–g) Difference of building height over each successive year.

Because of the difficulty in displaying results on a large scale at 10 m resolution, we created a vector grid with a resolution of 0.0125° to perform partition statistics on the original results. The sum of the building pixel heights within each grid is shown in Figure 6a–d. Between 2019 and 2022, the overall layout of buildings in Tianjin City did not undergo marked changes. However, fluctuations in building heights occurred in the core urban areas of Tianjin City over the four-year period. As depicted in Figure 6e–g, a decrease in overall building height was apparent from 2019 to 2020, followed by a substantial increase from 2020 to 2021, contrary to actual trends. Several factors might have contributed to these results. First, the characteristics of the random forest regression model itself and variations in sample distribution each year may cause fluctuations in building height regression results. Second, because of the limited number of samples for tall buildings, which constituted only a small portion of the total samples, the model's performance in predicting high-rise buildings exceeding 30 m in the core urban area was not as effective as that for general buildings below 30 m, further affecting the results in the core area.

Despite these influences, the results of this study clearly reflected the dynamic changes in building heights in rapidly developing areas. Noticeable increases in the building heights could be observed at the edges of the area, as depicted in Figure 6e–g. Moreover, in selected areas with more pronounced changes, a clear increasing trend was apparent (Figure 7). Specifically, the area covered by buildings in 2020 expanded compared to that in 2019, and building height markedly increased from 2020 to 2022. This finding highlights the ability of the developed methodology to provide crucial support for monitoring dynamic changes in urban buildings.

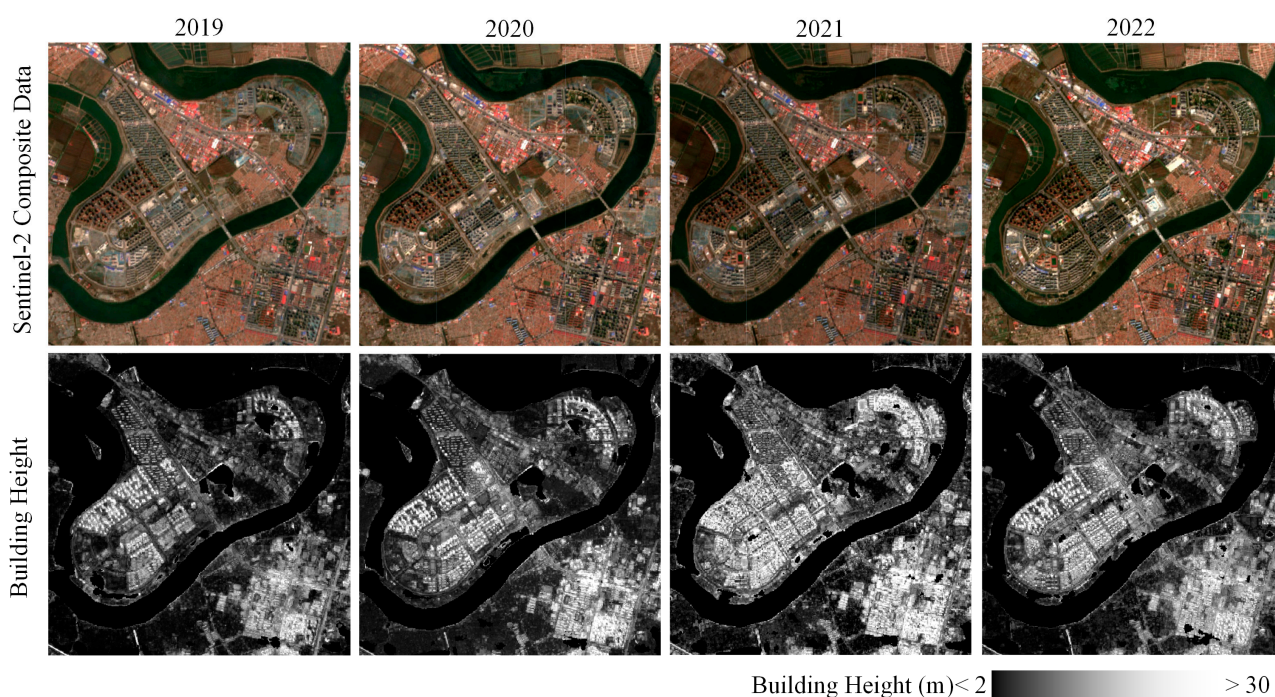


Figure 7. Satellite data-based estimation of building height in Ninghe District, Tianjin City. The first row shows the Sentinel-2 annual composite images from 2019 to 2022, whereas the second row displays the building height results for the same period.

3.3. Analysis of Building Height Dynamics

Because of the inherent variability of the random forest regression algorithm, the results of the building height regression for each year may not be entirely stable, resulting in different height assessments for the same building. However, this does not imply that the results are unsuitable for dynamic analysis, as the changes in building heights between the two years followed a normal distribution. We employed the three-sigma principle to

extract areas with significant changes in building height and conducted further analyses therein. Based on the different administrative divisions within Tianjin City, the changes in building height in different areas were then quantitated (Figure 8).

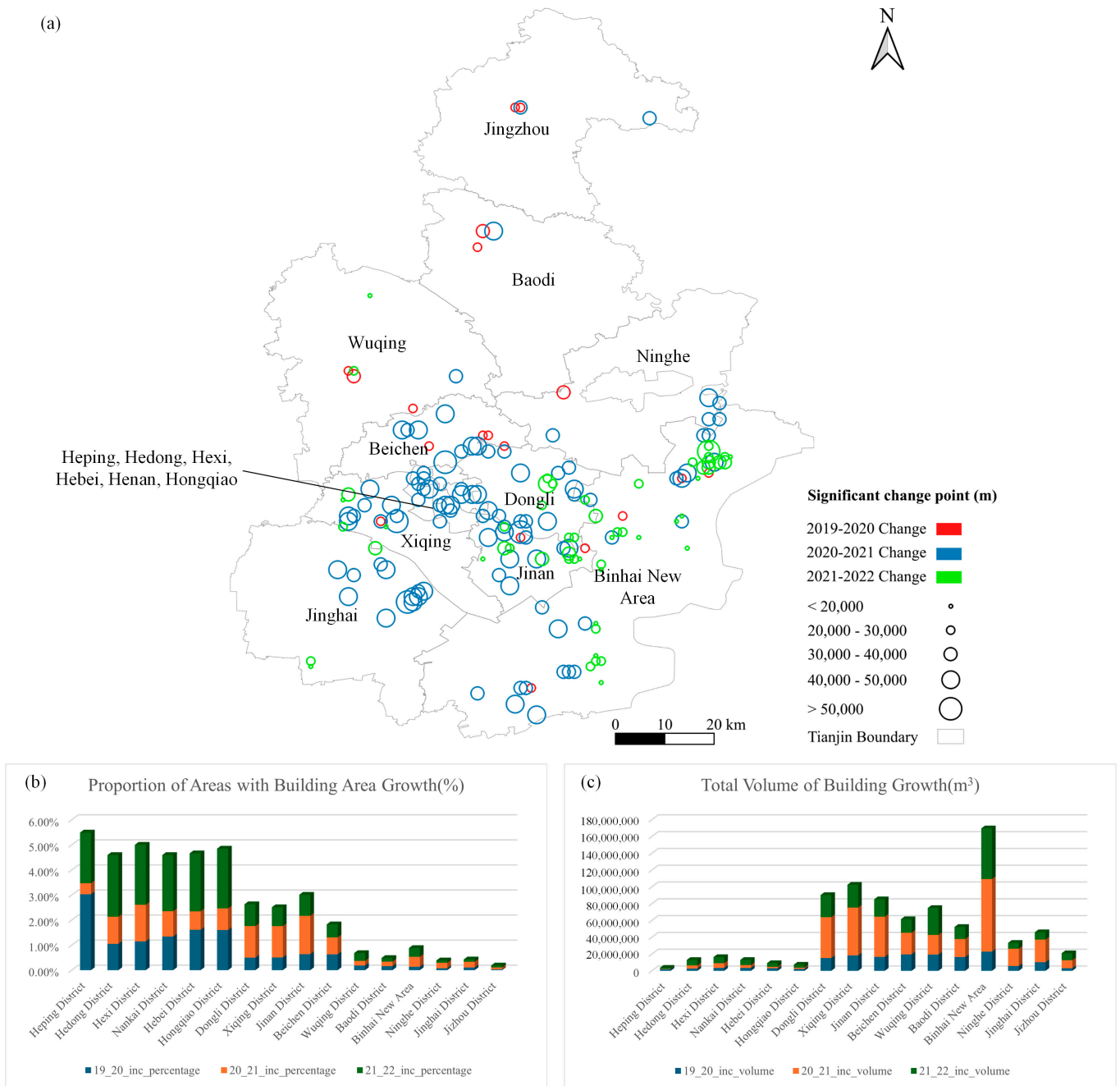


Figure 8. Building height change statistics. (a) Points where significant changes in building height occurred between each two-year period. (b,c) Statistics of changes in building area and volume for various administrative districts in Tianjin City.

Figure 8a presents numerous points indicative of substantial increases in building heights between 2020 and 2021. Figure 8b shows the total volume of building growth in each district of Tianjin City. The old urban areas of Tianjin, such as Heping District, have relatively small administrative areas, with only a 10.01 km² increase in building area. Moreover, owing to constraints on large-scale construction activities in old urban areas, the total volume of building growth from 2019 to 2022 was 1,898,205.784 m³ for Heping District,

356,749.394 and 1,317,668.213 m³, respectively. Compared to the substantial growth in the volume of construction in the emerging Binhai New Area over the same four-year period (22,856,517.3, 86,413,702.04, and 60,347,107.6 m³, respectively), the total construction volume in Heping District was relatively small. However, as shown in Figure 8c, the percentage increase in building area was higher in old urban than in new areas. For example, in Heping District and Binhai New Area, the percentage increases in building area from 2019 to 2022 were 3.0, 4.4, and 2.0%, and 0.13, 0.40, and 0.35%, respectively. In terms of the proportion of newly added building areas, the growth area in the Heping District accounted for 9.4% of the total area over the study period, whereas that in the Binhai New Area accounted for only 0.88%. Together, these results highlight the ability of the developed method to provide valuable insights regarding changes in building height over time.

3.4. Accuracy Assessment

In this study, we utilized the building height prediction output by the random forest regression model at a 10 m resolution, assigning the predicted heights to the corresponding positions within a raster grid. To validate the raster results, we sampled a 10% subset of the validation points that were separated from the reference data samples during the model construction, thereby obtaining pairs of predicted and true values. We conducted accuracy assessments for each year; the validation outcomes are presented in Figure 9.

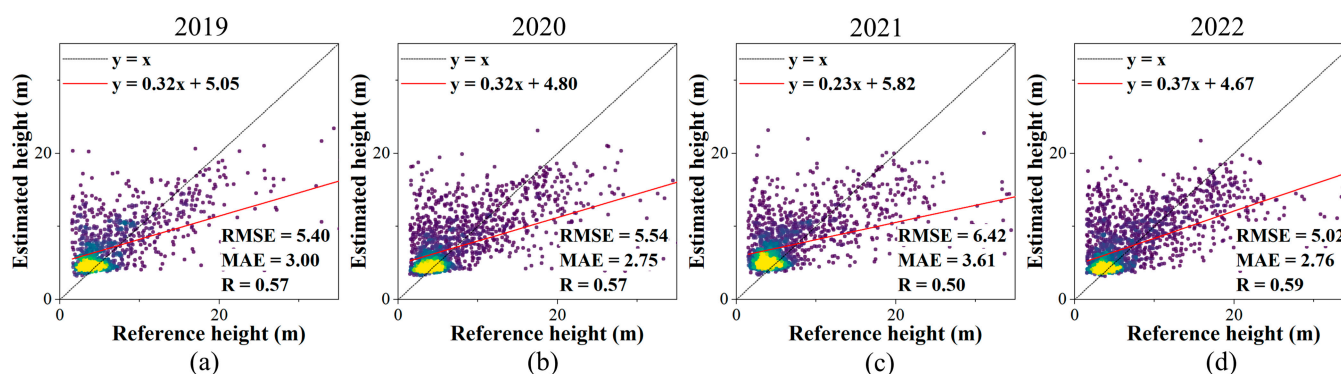


Figure 9. Accuracy validation of the building height calculations for each year. (a–d) Reference vs. estimated heights for 2019 to 2022. RMSE, root mean square error; MAE, mean absolute error, R, Pearson correlation coefficient.

The validation results reveal that the building height inversion outcomes for the years 2019 to 2022 consistently maintain MAEs below 3.61 m and RMSEs under 6.5 m, with average R, RMSE, and MAE values of 0.557, 5.59 m, and 3.03 m, respectively, substantiating the effectiveness of the developed method in achieving accurate building height estimation at the city scale. Nonetheless, the performance of this method is subject to variations in the quality of remote sensing imagery and the characteristics of ICESat-2 photons, including their quality and distribution, across different time periods. As a result, the annual inversion performance was not entirely consistent, with an average correlation coefficient of 0.557 over the four-year period, which was comparatively lower than that of the alternative methods.

3.5. Implications and Uncertainties

In comparison to previous studies, such as Wu et al. [38], who constructed 22,909 building height samples nationwide based on Baidu data, rendering updates challenging, the present study established a total of 70,612 evenly distributed samples in Tianjin over four years. The developed approach therefore not only overcomes the issue of constructing building height samples across multiple years, but also furnishes a vastly larger and higher precision sample base, highlighting the substantial potential of this method for

the dynamic monitoring of building heights in large cities. This study compares the results with the CNBH-10m building height dataset, as illustrated in Figure 10.

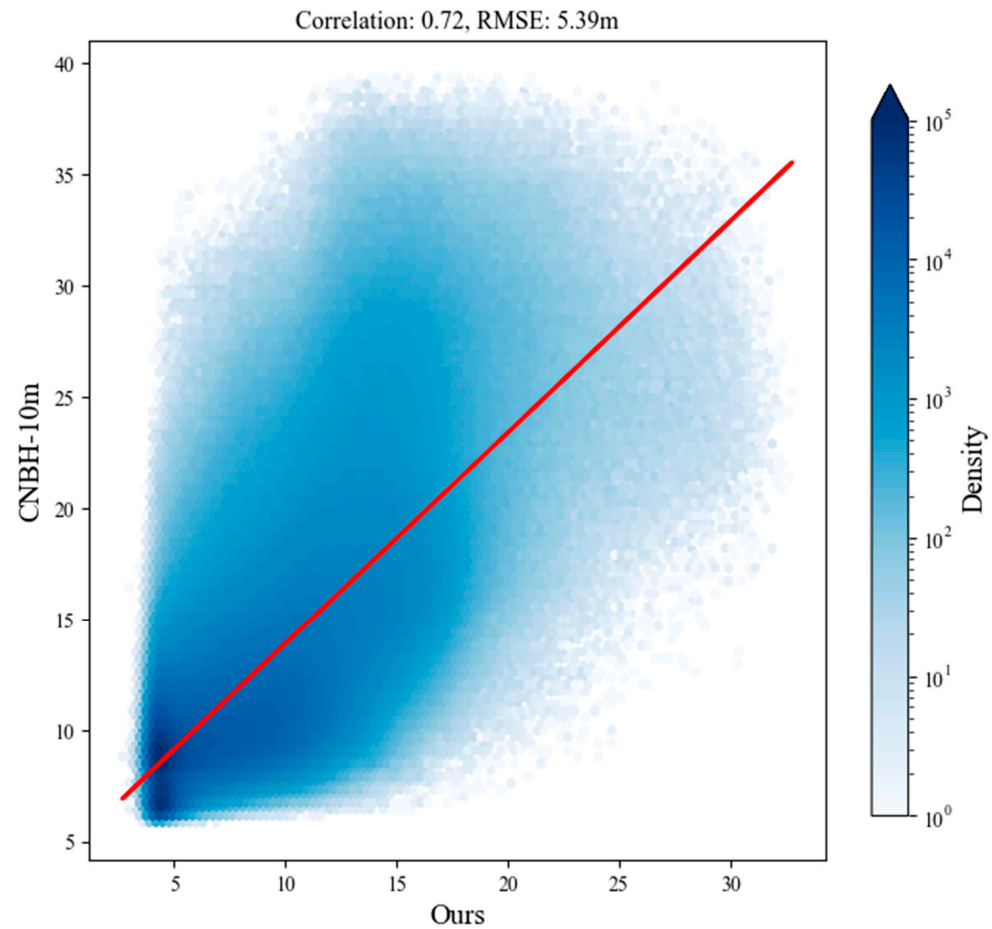


Figure 10. Comparison with CNBH-10m building height dataset. The comparison results indicate that the building heights calculated in this study exhibit a consistency of 0.72 with the CNBH-10m dataset, with an RMSE of 5.39 m. Considering that the ICESat-2 photon data designed for this study are challenging to frequently obtain elevation data within the range of high-rise buildings, the overall building height is likely to be underestimated compared to the CNBH-10m dataset. Consequently, the RMSE is relatively large, but the correlation remains strong. This demonstrates that the calculation results of this study have a high level of reliability.

Moreover, the sample construction methodology in this study relies on ICESat-2 satellite and building rooftop vector data. Since its launch in 2018, ICESat-2 has amassed a wealth of photon elevation point data worldwide, with the ATL03 product being updated every three months. Building rooftop vector data are also extensively produced and updated globally, encompassing datasets such as the Vectorized Rooftop Area Data for the 90 Cities in China [38] used in this study and Google’s MSBuildings, covering various regions worldwide. This implies that the proposed method can dynamically construct building height samples on a global scale. Crucially, neither type of dataset relies on ground-based manual surveys, affording a marked advantage when dealing with typically inaccessible regions, such as war zones or disaster-stricken areas. This facility aids in filling data gaps in global building height datasets and provides robust data support for assessing dynamic changes in urban 3D structures under the influence of wars, disasters, and other factors. Furthermore, it paves the way for establishing a long-term series of building height inversions on a global scale with promising applications.

This study has certain limitations. First, the construction of samples in this method relies on the assumption of continuous smoothness of building tops and the surrounding

ground, which introduces uncertainties when dealing with complex terrain or architecture. Second, the random forest regression method based on multi-source remote sensing data exhibited some instability. The height assessments of the same object may not be consistent across different periods, thereby increasing measurement errors and representing an issue necessitating further improvement. Finally, constrained by the temporal scale of the data, the current method can only achieve building height retrieval over four to five years. This is insufficient to support the long-term analysis of building height changes. Subsequent analyses will require the accumulation of data from ICESat-2, or the acquisition of new data from similar sensors.

4. Conclusions

This study proposed a method for dynamically retrieving building heights at a 10 m resolution in Tianjin City from 2019 to 2022 using satellite altimetry radar data and building rooftop contour data in conjunction with multisource optical remote sensing data, employing a random forest regression model. The accuracy of building height retrieval over multiple years was relatively high, with average R, RMSE, and MAE values of 0.557, 5.59 m, and 3.03 m, respectively. Significant changes in building height could be identified using the three-sigma principle.

The total volume of newly constructed buildings in the old urban areas of Tianjin City, such as the Heping District, was 3,572,623.3918 m³, markedly less than the additional volume in emerging urban areas, such as the Binhai New Area, which was 169,617,326.94 m³. However, in terms of the proportion of newly added building areas, the growth area in the Heping District accounted for 9.4% of the total area over the study period, whereas that in the Binhai New Area accounted for only 0.88%.

In summary, this study proposed a method for dynamically retrieving building heights at a 10 m resolution using ICESat-2 photon data and multisource optical remote sensing data, providing a reliable approach for analyzing the 3D structural dynamics of urban areas. Given the broad distribution and high update frequency of ICESat-2 photon data and building rooftop vector boundary data required for constructing building height samples on a global scale, this method holds enormous potential for the global dynamic retrieval of building heights, and offers a feasible means of observing building dynamics in remote and conflict regions where direct sampling is challenging.

Author Contributions: Conceptualization, H.X.; methodology, H.X., J.W. and J.Y. (Jiaqi Yao); investigation, L.G., W.J. and B.N.; writing—original draft preparation, H.X.; writing—review and editing, H.X., N.X., X.G., Y.L., J.Y. (Jianhua Yang) and J.Z. All authors have read and agreed to the published version of the manuscript.

Funding: This research was funded by the National Natural Science Foundation of China, grant number 42301501, the 2022 Tianjin Municipal Graduate Students' Scientific Research and Innovation Project, grant number 2022SKYZ270, and the National Natural Science Foundation of China, grant number 42101343.

Data Availability Statement: Data available on request from the authors.

Conflicts of Interest: The authors declare no conflicts of interest.

References

1. Ghaffarian, S.; Kerle, N.; Filatova, T. Remote sensing-based proxies for urban disaster risk management and resilience: A review. *Remote Sens.* **2018**, *10*, 1760. [[CrossRef](#)]
2. Kang, L.; Zhao, W.; Qi, B.; Banerjee, S. Augmenting self-driving with remote control: Challenges and directions. In Proceedings of the 19th International Workshop on Mobile Computing Systems & Applications, HotMobile '18, Tempe, AZ, USA, 12–13 February 2018; ACM: New York, NY, USA, 2018; pp. 19–24. [[CrossRef](#)]
3. Pham, H.M.; Yamaguchi, Y.; Bui, T.Q. A case study on the relation between city planning and urban growth using remote sensing and spatial metrics. *Landsc. Urban Plan.* **2011**, *100*, 223–230. [[CrossRef](#)]
4. Cai, Y.; Huang, H.; Wang, K.; Zhang, C.; Fan, L.; Guo, F. Selecting optimal combination of data channels for semantic segmentation in city information modelling (CIM). *Remote Sens.* **2021**, *13*, 1367. [[CrossRef](#)]

5. Qi, J.; Xie, D.; Yin, T.; Yan, G.; Gastellu-Etchegorry, J.P.; Li, L.; Zhang, W.; Mu, X.; Norford, L.K. LESS: Large-Scale remote sensing data and image simulation framework over heterogeneous 3D scenes. *Remote Sens. Environ.* **2019**, *221*, 695–706. [\[CrossRef\]](#)
6. Fuentes Reyes, M.; Xie, Y.; Yuan, X.; d'Angelo, P.; Kurz, F.; Cerra, D.; Tian, J. A 2D/3D multimodal data simulation approach with applications on urban semantic segmentation, building extraction and change detection. *ISPRS J. Photogramm. Remote Sens.* **2023**, *205*, 74–97. [\[CrossRef\]](#)
7. Li, W.; He, C.; Fang, J.; Zheng, J.; Fu, H.; Yu, L. Semantic segmentation-based building footprint extraction using very high-resolution satellite images and multi-source GIS data. *Remote Sens.* **2019**, *11*, 403. [\[CrossRef\]](#)
8. Rottensteiner, F.; Sohn, G.; Jung, J.; Gerke, M.; Baillard, C.; Benitez, S.; Breitkopf, U. The ISPRS benchmark on urban object classification and 3D building reconstruction. *ISPRS Ann. Photogramm. Remote Sens. Spat. Inform. Sci.* **2012**, *1-3*, 293–298. [\[CrossRef\]](#)
9. Li, D.; Yao, Y.; Shao, Z. Big data in smart city. *Geomat. Inf. Sci. Wuhan Univ.* **2014**, *39*, 631–640. [\[CrossRef\]](#)
10. Awrangjeb, M.; Ravanbakhsh, M.; Fraser, C.S. Automatic detection of residential buildings using LIDAR data and multispectral imagery. *ISPRS J. Photogramm. Remote Sens.* **2010**, *65*, 457–467. [\[CrossRef\]](#)
11. Liu, C.; Huang, X.; Wen, D.; Chen, H.; Gong, J. Assessing the quality of building height extraction from ZiYuan-3 multi-view imagery. *Remote Sens. Lett.* **2017**, *8*, 907–916. [\[CrossRef\]](#)
12. Strzabala, K.; Cwiakala, P.; Gruszcyński, W.; Puniach, E.; Matwij, W. Determining changes in building tilts based on UAV photogrammetry. *Measurement* **2022**, *202*, 111772. [\[CrossRef\]](#)
13. Zhang, C.; Cui, Y.; Zhu, Z.; Jiang, S.; Jiang, W. Building height extraction from GF-7 satellite images based on roof contour constrained stereo matching. *Remote Sens.* **2022**, *14*, 1566. [\[CrossRef\]](#)
14. Zhao, C. Temporal and Spatial Differentiation Characteristics of the Three-Dimensional Landscape Pattern in Jinan City. Master's Thesis, Shandong Normal University, Jinan, China, 2019.
15. Cao, Y.; Huang, X. A deep learning method for building height estimation using high-resolution multi-view imagery over urban areas: A case study of 42 Chinese cities. *Remote Sens. Environ.* **2021**, *264*, 112590. [\[CrossRef\]](#)
16. Xu, M.; Cao, C.; Jia, P. Mapping fine-scale urban spatial population distribution based on high-resolution stereo pair images, points of interest, and land cover data. *Remote Sens.* **2020**, *12*, 608. [\[CrossRef\]](#)
17. Wang, J.; Hu, X.; Meng, Q.; Zhang, L.; Wang, C.; Liu, X.; Zhao, M. Developing a method to extract building 3D information from GF-7 data. *Remote Sens.* **2021**, *13*, 4532. [\[CrossRef\]](#)
18. Ruan, Y.; Cai, G.; Xue, Y. Optimization of urban elevation accuracy by combining laser altimetry and stereoscopic imaging. In Proceedings of the 2023 IEEE International Geoscience and Remote Sensing Symposium, Pasadena, CA, USA, 16–21 July 2023; IEEE: New York, NY, USA, 2023; pp. 3686–3689. [\[CrossRef\]](#)
19. Du, X.; Wang, L.; Tang, F.; Xu, S.; Muhammad, S.; Nath, B.; Niu, Z. Estimation and development-potential analysis of regional housing in Ningbo City based on high-resolution stereo. *Remote Sens.* **2023**, *15*, 3953. [\[CrossRef\]](#)
20. Abdela, N. Deep Learning-Based Digital Surface Model (DSM) Generation Using SAR Image and Building Footprint Data. Master's Thesis, University of Twente, Enschede, The Netherlands, 2023.
21. Zhang, Y.; Wang, M.; Wan, Y.; Zhou, B.; Feng, J.; Cao, B.; Yao, Y. Compensation model of GF-7 panchromatic and multispectral image registration error. *Geomat. Inform. Sci. Wuhan Univ.* **2023**, *48*, 1029–1038. [\[CrossRef\]](#)
22. Ma, X.; Zheng, G.; Xu, C.; Moskal, L.M.; Gong, P.; Guo, Q.; Huang, H.; Li, X.; Pang, Y.; Wang, C.; et al. A global product of fine-scale urban building height based on spaceborne lidar. *arXiv* **2023**, arXiv:2310.14355. [\[CrossRef\]](#)
23. Zhang, J.; Kerekes, J.; Csatho, B.; Schenk, T.; Wheelwright, R. A clustering approach for detection of ground in micropulse photon-counting LiDAR altimeter data. In Proceedings of the 2014 IEEE Geoscience and Remote Sensing Symposium, Quebec City, QC, Canada, 13–18 July 2014; IEEE: New York, NY, USA, 2014; pp. 177–180. [\[CrossRef\]](#)
24. Moussavi, M.S.; Abdalati, W.; Scambos, T.; Neuenschwander, A. Applicability of an automatic surface detection approach to micro-pulse photon-counting lidar altimetry data: Implications for canopy height retrieval from future ICESat-2 data. *Int. J. Remote Sens.* **2014**, *35*, 5263–5279. [\[CrossRef\]](#)
25. Chen, B.; Pang, Y.; Li, Z.; Lu, H.; North, P.; Rosette, J.; Yan, M. Forest signal detection for photon counting LiDAR using random forest. *Remote Sens. Lett.* **2020**, *11*, 37–46. [\[CrossRef\]](#)
26. Xu, N.; Ma, X.; Ma, Y.; Zhao, P.; Yang, J.; Wang, X.H. Deriving highly accurate shallow water bathymetry from Sentinel-2 and ICESat-2 datasets by a multitemporal stacking method. *IEEE J. Sel. Top. Appl. Earth Obs. Remote Sens.* **2021**, *14*, 6677–6685. [\[CrossRef\]](#)
27. Dandabathula, G.; Hari, R.; Ghosh, K.; Bera, A.K.; Srivastav, S.K. Accuracy assessment of digital bare-earth model using ICESat-2 photons: Analysis of the FABDEM. *Model. Earth Syst. Environ.* **2023**, *9*, 2677–2694. [\[CrossRef\]](#)
28. Gu, L.; Fan, D.; Ji, S.; Gong, Z.; Li, D.; Dong, Y. Signal photon extraction method for ICESat-2 data using slope and elevation information provided by stereo images. *Sensors* **2023**, *23*, 8752. [\[CrossRef\]](#) [\[PubMed\]](#)
29. Ma, Y.; Zhang, W.; Sun, J.; Li, G.; Wang, X.H.; Li, S.; Xu, N. Photon-counting lidar: An adaptive signal detection method for different land cover types in coastal areas. *Remote Sens.* **2019**, *11*, 471. [\[CrossRef\]](#)
30. Zhao, Y.; Wu, B.; Shu, S.; Yang, L.; Wu, J.; Yu, B. Evaluation of ICESat-2 ATL03/08 surface heights in urban environments using airborne LiDAR point cloud data. *IEEE Geosci Remote Sens. Lett.* **2021**, *19*, 7002905. [\[CrossRef\]](#)
31. Lao, J.; Wang, C.; Zhu, X.; Xi, X.; Nie, S.; Wang, J.; Cheng, F.; Zhou, G. Retrieving building height in urban areas using ICESat-2 photon-counting LiDAR data. *Int. J. Appl. Earth Obs. Geoinf.* **2021**, *104*, 102596. [\[CrossRef\]](#)

32. Dandabathula, G.; Sitiraju, S.R.; Jha, C.S. Retrieval of building heights from ICESat-2 photon data and evaluation with field measurements. *Environ. Res. Infrastruct. Sustain.* **2021**, *1*, 011003. [[CrossRef](#)]
33. Yao, J.; Tang, Z.; Li, G.; Chen, J.; Zuo, Z.; Ai, B.; Zhang, S.; Guo, J. Influence of atmospheric scattering on the accuracy of laser altimetry of the GF-7 satellite and corrections. *Remote Sens.* **2021**, *14*, 129. [[CrossRef](#)]
34. Tang, X.; Yao, J.; Chen, J.; Li, G.; Zhang, W. Multimodel fusion method for cloud detection in satellite laser footprint images. *IEEE Geosci Remote Sens. Lett.* **2022**, *19*, 6513905. [[CrossRef](#)]
35. Li, G.; Yao, J.; Tang, X.; Ding, B.; Guo, J.; Zuo, Z.; Chen, J.; Liu, Z. Research on automatic extraction method for laser elevation control points of GF-7 satellite. In Proceedings of the 8th China High Resolution Earth Observation Conference, Beijing, China, 16 May 2023; Wang, L., Wu, Y., Gong, J., Eds.; Springer: Singapore, 2023. [[CrossRef](#)]
36. Harding, D.J.; Yang, G.; Chen, J.; Stephen, M.; Mackinnon, J.P.; Ranson, J.; Dabney, P. Technology maturation for the decadal survey Surface Topography and Vegetation (STV) observable: Concurrent Artificially-intelligent Spectrometry and Adaptive Lidar System (CASALS). In Proceedings of the AGU Fall Meeting, Chicago, IL, USA, 12–16 December 2022; AGU: Washington, DC, USA, 2022; p. GC15F-07.
37. Zhao, Y.; Wu, B.; Li, Q.; Yang, L.; Fan, H.; Wu, J.; Yu, B. Combining ICESat-2 photons and Google Earth Satellite images for building height extraction. *Int. J. Appl. Earth Observ. Geoinform.* **2023**, *117*, 103213. [[CrossRef](#)]
38. Wu, B.; Huang, H.; Zhao, Y. Utilizing building offset and shadow to retrieve urban building heights with ICESat-2 photons. *Remote Sens.* **2023**, *15*, 3786. [[CrossRef](#)]
39. Zhou, X.; Myint, S.W. Shadow pattern-enhanced building height extraction using very-high-resolution image. *IEEE J. Sel. Top. Appl. Earth Obs. Remote Sens.* **2022**, *16*, 180–190. [[CrossRef](#)]
40. TPDC. *Vectorized Rooftop Area Data for 90 Cities in China (2020)*; National Tibetan Plateau/Third Pole Environment Data Center: Beijing, China, 2021. [[CrossRef](#)]
41. Liu, M.; Ma, J.; Zhou, R.; Li, C.; Li, D.; Hu, Y. High-resolution mapping of mainland China's urban floor area. *Landsc. Urban Plan.* **2021**, *214*, 104187. [[CrossRef](#)]

Disclaimer/Publisher's Note: The statements, opinions and data contained in all publications are solely those of the individual author(s) and contributor(s) and not of MDPI and/or the editor(s). MDPI and/or the editor(s) disclaim responsibility for any injury to people or property resulting from any ideas, methods, instructions or products referred to in the content.